

Brightness temperature constraints from interferometric visibilities

Andrei Lobanov^{1,2}

¹ Max-Planck-Institut für Radioastronomie, Auf dem Hügel 69, 53121 Bonn, Germany

² Institut für Experimentalphysik, Universität Hamburg, Luruper Chaussee 149, 22761 Hamburg, Germany

Received 1 October 2014 / Accepted 4 December 2014

ABSTRACT

Context. The brightness temperature is an effective parameter that describes the physical properties of emitting material in astrophysical objects. It is commonly determined by imaging and modeling the structure of the emitting region and estimating its flux density and angular size.

Aims. Reliable approaches for visibility-based estimates of brightness temperature are needed for interferometric experiments in which poor coverage of spatial frequencies prevents successful imaging of the source structure, for example, in interferometric measurements made at millimeter wavelengths or with orbiting antennas.

Methods. Such approaches can be developed by analyzing the relations between brightness temperature and visibility amplitude and its r.m.s. error.

Results. A method is introduced for directly calculating the lower and upper limits of the brightness temperature from visibility measurements. The visibility-based brightness temperature estimates are shown to agree well with the image-based estimates obtained in the 2 cm MOJAVE survey and the 3 mm CMVA survey, with good agreement achieved for interferometric measurements at spatial frequencies exceeding $\approx 2 \times 10^8$.

Conclusions. The method provides an essential tool for constraining brightness temperature in all interferometric experiments with poor imaging capability.

Key words. methods: analytical – techniques: interferometric – galaxies: jets

1. Introduction

Interferometric measurements offer a powerful tool for probing the finest structures of emitting objects by extending the effective instrumental diameter to the maximum distance (baseline length) between individual elements of an interferometer. However, for interferometric measurements made at extreme baseline lengths, imaging the structure of the target object becomes increasingly limited owing to incomplete sampling of the Fourier plane. This is often the case in radio interferometric measurements made with very long baseline interferometry (VLBI) at millimeter wavelengths (*cf.* Doeleman et al. 2012) and with space-ground interferometers such as VSOP (Horiuchi et al. 2004) or RadioAstron (Kardashev et al. 2013). In these situations, more basic measurements of flux density, S_ν , and emitting area, Ω , of the structure can still be obtained (*i.e.*, from model fitting of the visibility distribution) and can be combined to yield a brightness temperature estimate. The latter can then be used as a generic indicator of the physical conditions of the emitting material (*cf.* Lobanov et al. 2000; Kovalev et al. 2005; Homan et al. 2006; Lee et al. 2008).

For the black-body spectrum in the Rayleigh-Jeans limit ($h\nu \ll kT$), the brightness, I_ν , is approximated by $I_\nu = 2\nu^2 kT/c^2$, and the respective brightness temperature is $T_b = I_\nu c^2/(2k\nu^2)$, where h and k are the Planck and Boltzmann constants, respectively, and c is the speed of light. In terms of the measured quantities, S_ν and Ω , the resulting brightness is $I_\nu = S_\nu/\Omega = S_\nu/[2\pi(1 - \cos\rho_d)]$, if the emitting region is a uniformly bright circle of angular radius ρ_d . For small ρ_d , the term $1 - \cos\rho_d$ is approximated by $\rho_d^2/2$, which yields $I_\nu \approx S_\nu/(\pi\rho_d^2)$. If the emitting region is unresolved, ρ_d can be constrained by the

resolution limit, θ_{lim} , of the measurement, providing lower limits on the brightness, $I_\nu \geq 4S_\nu/(\pi\theta_{\text{lim}}^2)$, and brightness temperature, $T_b \geq 2S_\nu c^2/(\pi k\nu^2\theta_{\text{lim}}^2)$.

In absence of information about the actual brightness distribution of emission in a compact, marginally resolved region, it is often assumed that it can be represented satisfactorily by a two-dimensional Gaussian distribution described by a flux density S_g and respective major and minor axes θ_{maj} and θ_{min} . This translates into $I_\nu = (4 \ln 2/\pi) S_g/(\theta_{\text{maj}}\theta_{\text{min}})$ and $T_b = [2 \ln 2/(\pi k)] S_g c^2/(\nu^2 \theta_{\text{maj}}\theta_{\text{min}})$. These expressions are used for the bulk of brightness temperature estimates based on decomposition of the observed structure into one or more two-dimensional Gaussian features (Gaussian components). Several other analytical patterns of brightness distribution patterns have been employed to analyze different astrophysical objects (*cf.* Berger 2003) such as resolved stars (Dyck et al. 1998; Ohnaka et al. 2013), young supernovae (Marcaide et al. 2009), recurrent novae (Chesneau et al. 2007), protoplanetary disks (Malbet et al. 2005), or active galaxies (Weigelt et al. 2012). In all of these cases, successful fitting of a given brightness distribution pattern to visibility data is a strong prerequisite for recovering structural and physical information about the target object.

However, the most extreme cases of interferometric observations, such as millimeter and space VLBI measurements, often do not provide enough data to warrant reliable model fitting owing to lack of short-baseline measurements and the complexity of the fine structure in most of the targets. These observations require a different approach for estimating the brightness temperature. In this paper, such an approach is proposed based on individual visibility measurements and their errors (which can be

reliably estimated in most of the measurements). The methodology of this approach is described in Sect. 2 and is tested with the visibility data from two VLBA¹ observations of the prominent compact radio sources 3C 345 and NGC 1052. Applications of the visibility-based T_b estimates are discussed in Sect. 3 and are compared with the results from the 3 mm CMVA² and 2 cm MOJAVE³ surveys and in connection with an analysis of space VLBI and millimeter VLBI surveys of compact radio sources. Additional potential applications of the method to other types of astrophysical targets are also discussed, and expressions for brightness temperature limits for several specific brightness distribution patterns are presented in the appendix.

2. Brightness temperature limits from interferometric visibilities

We consider an emitting region with a brightness distribution, I_r , observed instantaneously at a wavelength, λ , by an interferometer consisting of two receiving elements (telescopes) separated by a baseline distance, B . This observation corresponds to measuring the Fourier transform of I_r at a single spatial (Fourier) frequency $q = B/\lambda$ (also called uv distance or uv radius). It yields an interferometric visibility, $V = V_q e^{-i\phi_q}$, described by its amplitude V_q and phase ϕ_q , and their respective errors σ_q and σ_ϕ . Generally speaking, V_q depends on the shape and angular extent of the brightness distribution, and $\phi_q = \phi_p + \phi_o$ is a function of its position and geometry. The position-dependent term of the phase, ϕ_p , is relative and can always be zeroed by an appropriate shift applied to the visibility (which is analogous to re-pointing the interferometer). The geometry-dependent term of the phase, ϕ_o , depends on the structure of the brightness distribution and its orientation with respect to the projection of the interferometric baseline on the picture plane. For a circularly symmetric or axially symmetric brightness distribution, $\phi_o \equiv 0$, independently of the baseline orientation.

2.1. Minimum brightness temperature

Without *a priori* information about the specific structural shape of I_r , the symmetry assumption can be employed and the angular extent of the emission can be estimated from V_q alone. This assumption is routinely used for size and brightness temperature estimates made from interferometric data (*cf* Lobanov et al. 2000; Kovalev et al. 2005; Lee et al. 2008).

Such estimates require knowledge of the *zero-spacing* visibility, V_0 , and rely upon assumption of a specific symmetric template for I_r . For instance, for a circular Gaussian distribution, the respective expression for V_q is

$$V_q = V_0 \exp\left(-\frac{\pi^2 \theta_r^2 q^2}{4 \ln 2}\right)$$

and it can be used for obtaining an estimate of the size, θ_r , of the emitting region:

$$\theta_r = \frac{2 \sqrt{\ln 2}}{\pi} \frac{\lambda}{B} \sqrt{\ln(V_0/V_q)}. \quad (1)$$

¹ Very Long Baseline Array of National Radio Astronomy Observatory, Socorro NM, USA; <http://www.nrao.edu>

² Coordinated Millimeter VLBI Array, currently succeeded by the Global Millimeter VLBI Array; <http://www3.mpifr-bonn.mpg.de/div/vlbi/globalmm/>

³ <http://www.physiscs.purdue.edu/astro/MOJAVE/>

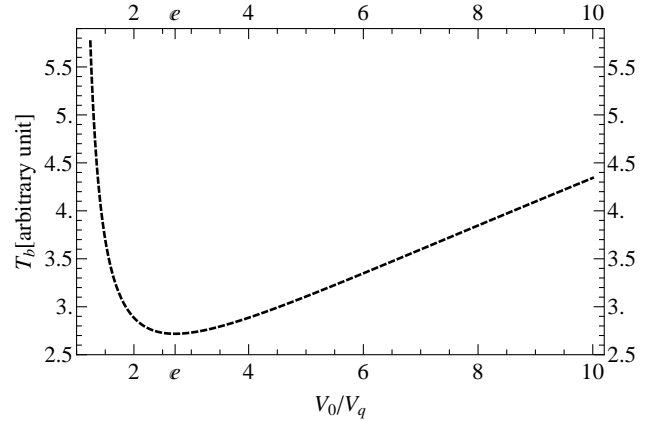


Fig. 1. Brightness temperature in relative units as a function of the ratio V_0/V_q between the zero-spacing flux density and visibility flux density measured at a given spatial frequency q , assuming that the brightness distribution is Gaussian. The lowest value of the brightness temperature is realized with the ratio $V_0/V_q = e$.

With this expression, the brightness temperature can be estimated from

$$T_b = \frac{\pi}{2k} \frac{B^2 V_0}{\ln(V_0/V_q)}. \quad (2)$$

Appendix A lists the respective expressions derived for several other patterns of brightness distributions commonly used in the analysis of astronomical data.

Equation 2 provides the lowest value of T_b for $V_0 = e V_q$ (see Fig. 1), which yields an estimate of the *minimum brightness temperature* supported by the measured visibility amplitude V_q :

$$T_{b,\min} = \frac{\pi e}{2k} B^2 V_q \approx 3.09 \left(\frac{B}{\text{km}}\right)^2 \left(\frac{V_q}{\text{mJy}}\right) [\text{K}]. \quad (3)$$

This expression describes the *absolute minimum* of the brightness temperature that can be obtained from the measured visibility amplitude V_q under the assumption that the brightness distribution is well approximated by a circular Gaussian. The lowest brightness temperature is realized for any visibility distribution that has an inflection point. The respective expressions of $T_{b,\min}$ for other patterns of brightness distributions are listed in Appendix A.

2.2. Maximum measurable brightness temperature

The expression for $T_{b,\min}$ given by Eq. 3 is independent of V_0 , while estimating the *maximum* brightness temperature will necessarily require knowledge, or at least a reasonable assumption, of V_0 . With the latter, it should be kept in mind that if only a limit on V_0 can be assumed, the nature of the resulting estimate of T_b depends on the ratio of V_0/V_q . The maximum T_b can only be derived from *upper* limits on V_0 for $V_0 > e V_q$ and from *lower* limits on V_0 for $V_0 < e V_q$. In the opposite cases, the combination of V_0 and V_q yields an estimate of the *minimum* brightness temperature.

The zero-spacing visibility V_0 is often approximated by the total flux density, S_{tot} , measured at a single receiving element. Generally, this is a poor approximation because S_{tot} contains contributions from all angular scales. A better constraint on V_0

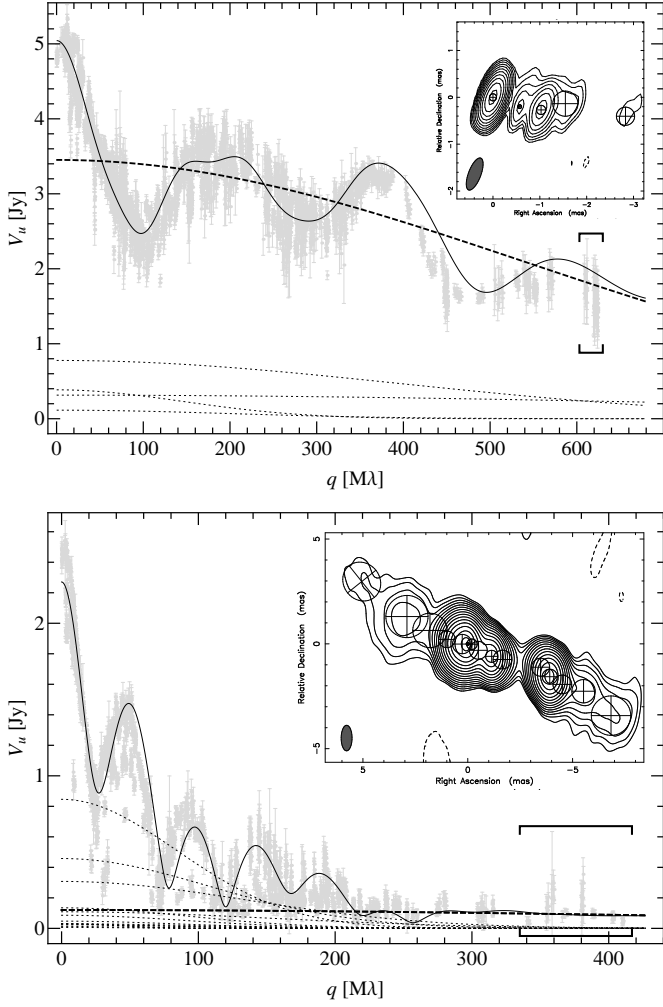


Fig. 2. Comparison of the visibility amplitude distribution and Gaussian model fit representation of the compact structure in a compact structure-dominated object (top, a 22 GHz VLBA observation of the quasar 3C 345 made on 23/08/1999) and an extended structure-dominated object (bottom, a 15 GHz VLBA observation of the radio galaxy NGC 1052 from MOJAVE Survey, made on 16/12/1995; Kellermann et al. 2004). The visibility amplitude distributions are projected onto a P.A. of -104° (3C 345) and -110° (NGC 1052) for illustration purposes, enabling a representation by a single, composite model fit rather than by fits to individual baselines. The insets show Gaussian model fit images of the source structure, with component locations and sizes indicated. The resulting fits of the visibility amplitudes are shown by the solid curves. The dotted curves show visibility representations of the individual model fit components. The thick dashed lines correspond to the respective visibility responses from the most compact “core” component that has the highest brightness temperature. Braces indicate the spatial frequency (uv distance) ranges in which the contribution from the core component dominates the measured visibility amplitude distribution (the uv ranges are measured in units of $M\lambda$, where λ is the observing wavelength). These spatial frequency ranges are best suited to directly estimate the brightness temperature from the visibility measurements.

is provided by the flux density of a respective Gaussian component if the data warrant reliable Gaussian decomposition. For extremely poor coverages of the Fourier domain, this is not the case, and no satisfactory estimate of V_0 can be made.

In this situation, a lower limit of $V_0 = V_q + \sigma_q$ can be adopted. This limit effectively corresponds to requiring that V_q

probes a structural detail that is marginally resolved (we recall that $V_q \equiv \text{const}$ results from the Fourier transform of a point source). This assumption is well justified for visibility measurements made at sufficiently long baselines, where the visibility amplitude is dominated by the most compact structure observed in the target object. It can furthermore be verified through the observed absence of amplitude beating at slightly shorter baselines (with the latter reflecting the presence of multiple compact emitting regions in the object). Examples of visibility (baseline) ranges dominated by contributions from the most compact structures are shown in Fig. 2 for two radio sources (NGC 1052 and 3C 345) that represent the typical cases of a compact radio source with and without a strong contribution from extended emission.

The requirement of marginal resolution of the observed structure implies that its size should be larger than

$$\theta_{\text{lim}} = \frac{2\sqrt{\ln 2}}{\pi} \frac{\lambda}{B} \sqrt{\ln \frac{V_q + \sigma_q}{V_q}}. \quad (4)$$

Correspondingly, the brightness temperature of this feature should not exceed the limit of

$$\begin{aligned} T_{b,\text{lim}} &= \frac{\pi B^2 (V_q + \sigma_q)}{2k} \left[\ln \frac{V_q + \sigma_q}{V_q} \right]^{-1} \\ &= 1.14 \left(\frac{V_q + \sigma_q}{\text{mJy}} \right) \left(\frac{B}{\text{km}} \right)^2 \left(\ln \frac{V_q + \sigma_q}{V_q} \right)^{-1} [\text{K}]. \end{aligned} \quad (5)$$

For visibilities with a signal-to-noise ratio $V_q/\sigma_q > e - 1$, the estimate of $T_{b,\text{lim}}$ provides the highest brightness temperature that can be obtained from the measured visibility amplitude and its error while requiring that the respective brightness distribution is a) circularly Gaussian, and b) marginally resolved by the measured visibility. Expressions for $T_{b,\text{lim}}$ derived for several other brightness distribution patterns are given in Appendix A.

As measurements of V_q and σ_q are made over extended time intervals, they correspond to averaging the visibility function over finite ranges of spatial frequencies (Δq , $\Delta\psi$), with ψ describing the positional angle of V_q in the Fourier plane. In this case, the estimate provided by Eq. 5 holds for as long as the condition $V_{q,\psi} \approx \text{const}$ is satisfied over the given measurement interval $[\Delta q, \Delta\psi]$. This condition effectively requires that the measured V_q is dominated by a contribution from a single emitting region that is marginally resolved at the spatial frequency q .

Equations 3 and 5 provide a robust bracketing for the brightness temperature obtained from interferometric measurements that have a limited sampling of the visibility distribution of the target. This can be demonstrated by applying these equations to every visibility of the VLBI datasets used in the examples shown in Fig. 2. Results of this application are presented in Fig. 3, where the visibility-based estimates of $T_{b,\text{min}}$ and $T_{b,\text{lim}}$ are plotted against the spatial frequency (uv radius) of the respective visibilities. These estimates can be compared with the brightness temperature, $T_{b,\text{mod}}$ estimated from the model fit parameters of the “core” component. This comparison indicates that at uv radii $\gtrsim 150 M\lambda$, the interval $[T_{b,\text{min}}, T_{b,\text{lim}}]$ represents a reasonably good bracketing for the expected maximum brightness temperature. This substantially exceeds the conservative expectations for the uv ranges (indicated by braces in Fig. 3) suitable for estimating the brightness temperature. Within these ranges, the average $T_{b,\text{lim}}$ is only marginally (factors of 1.5 and 2.2) higher than the $T_{b,\text{mod}}$ obtained from model fits. Hence, $T_{b,\text{lim}}$ estimates made at

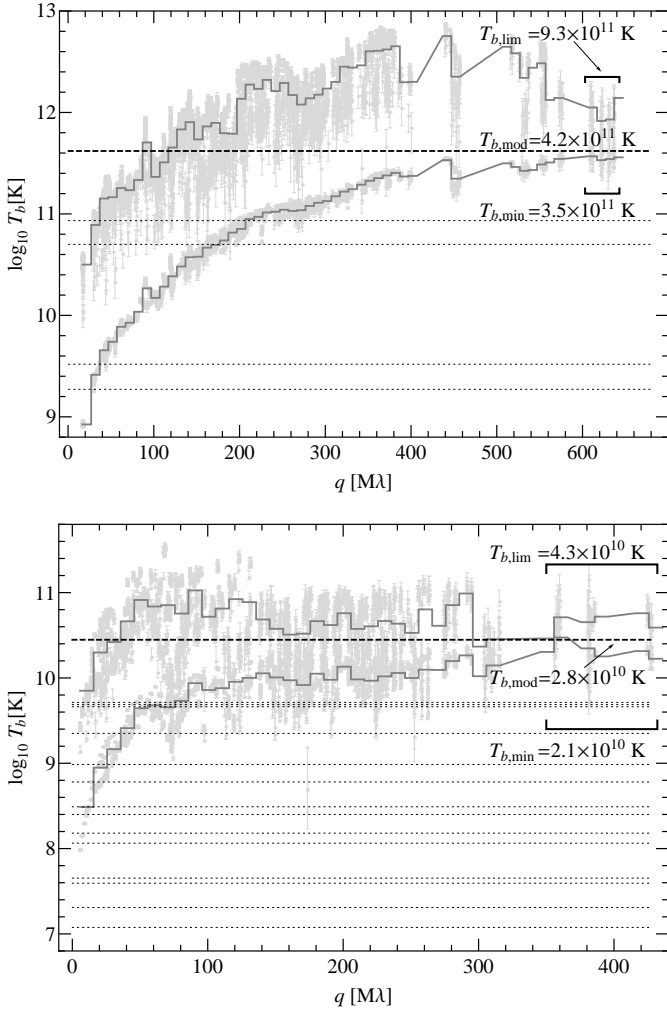


Fig. 3. Limiting, $T_{b,\text{lim}}$ (top row of datapoints) and minimum, $T_{b,\text{min}}$ (bottom row of datapoints), brightness temperature estimated directly from visibility data for 3C 345 (top panel) and NGC 1052 (bottom panel), plotted against the spatial frequency q (uv radius). The estimated values are compared with the brightness temperatures of the Gaussian model fit components (dotted lines for the jet components, thick dashed line for the core component) used to describe the source structure as shown in Fig. 2. Running stairs show the respective rows of the brightness temperature averaged within radial bins of $10\text{ M}\lambda$ in extent. Both the original and the averaged rows of the brightness temperature indicate that at $q \gtrsim 150\text{ M}\lambda$, the interval $[T_{b,\text{min}}, T_{b,\text{lim}}]$ provides a good bracketing for the maximum brightness temperature in each of the two objects. Braces indicate the conservative ranges of spatial frequency q identified as ranges dominated by the most compact part of the source structure. Averages of $T_{b,\text{min}}$ and $T_{b,\text{lim}}$ made over these ranges constrain the respective $T_{b,\text{mod}}$ estimates well.

long baselines can constrain the maximum brightness temperature well in both core-dominated and jet-dominated compact radio sources.

2.3. Corrections for elongation of the emitting region

The estimates of $T_{b,\text{min}}$ and $T_{b,\text{lim}}$ can furthermore be refined if the potential elongation of the emitting region is considered. If visibility measurements are made over a narrow range of position angle ψ in the Fourier plane, this elongation may bias individual estimates of the brightness temperature and introduce

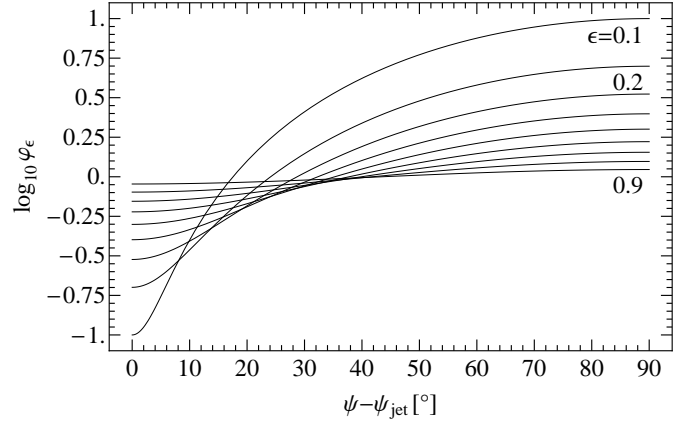


Fig. 4. Brightness temperature correction to account for the elongation of the emitting region. The elongated region is described by an elliptical Gaussian with an axial ratio ϵ . The corrections are plotted against the difference between the position angle of a visibility measurement and the position angle of the major axis of the Gaussian. Different curves correspond to the corrections for values of ϵ taken in steps of 0.1 between $\epsilon = 0.1$ and $\epsilon = 0.9$.

scatter in the statistics obtained from object samples. Gaussian modeling of fine structure in the objects from the MOJAVE sample (Kovalev et al. 2005) indicates that the core components are well described by elliptical Gaussian patterns, with an average elongation (minor to major axis ratio, $\epsilon = \theta_{\text{min}}/\theta_{\text{maj}}$) of 0.4 ± 0.2 . For visibility measurements made at a random position angle ψ (hence oriented randomly with respect to the source elongation), the resulting scatter of T_b estimates can approach one order of magnitude. This adverse effect of the source elongation can be taken into account in objects with a known elongation and position angle of the compact structure.

The compact core region can be approximated by an elliptical Gaussian with an axial ratio, ϵ , and a position angle of the major axis, ψ_{jet} . The angular size estimate, θ_r , obtained under the assumption of a circular Gaussian brightness distribution (e.g., with Eq. 1) can then be related to the major and minor axes of the elliptical Gaussian,

$$\begin{aligned}\theta_{\text{maj}} &= \theta_r / \sqrt{\sin^2 \zeta + \epsilon^2 \cos^2 \zeta}, \\ \theta_{\text{min}} &= \theta_r / \sqrt{\cos^2 \zeta + \epsilon^{-2} \sin^2 \zeta} \equiv \theta_{\text{maj}} \epsilon,\end{aligned}$$

where $\zeta = \psi - \psi_{\text{jet}}$ describes the difference between the visibility position angle and that of the major axis of the elliptical Gaussian component (hence $\theta_r = \theta_{\text{min}}$ for $\zeta = 0^\circ$ and $\theta_r = \theta_{\text{maj}}$ for $\zeta = 90^\circ$). For the brightness temperature estimates, this results in a multiplicative correction factor

$$\varphi_\epsilon = \theta_r^2 / (\theta_{\text{maj}} \theta_{\text{min}}) = \epsilon \cos^2 \zeta + \epsilon^{-1} \sin^2 \zeta \quad (6)$$

that should be applied to $T_{b,\text{min}}$ and $T_{b,\text{lim}}$ given by Eqs. 3 and 5. The magnitude of this correction is on the order of $1/\epsilon^2$ over the full range of values of ζ (see Fig. 4). Applying this correction may be particularly useful to analyze space VLBI measurements made with RadioAstron at baselines in excess of ten Earth diameters (hence falling within a range of $\Delta\psi \lesssim 6^\circ$). Other potential applications include snapshot VLBI measurements made at millimeter wavelengths (e.g., Doeleman et al. 2012; Petrov et al. 2012; Lee et al. 2013).

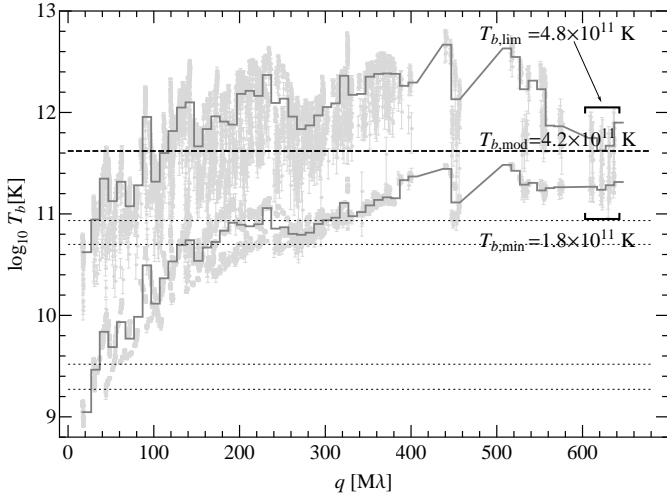


Fig. 5. The limiting, $T_{b,\text{lim}}$ (top run) and minimum, $T_{b,\text{min}}$ (bottom run), brightness temperature estimated directly from visibility data for 3C 345 and corrected for an assumed ellipticity of the emitting region, with $\epsilon = 0.5$ (based on MOJAVE model fitting reported in Kovalev et al. 2005), and $\psi_{\text{jet}} = -104^\circ$. The limiting brightness temperature of 4.8×10^{11} K, obtained from the visibilities at the longest baselines ($B > 600 \text{ M}\lambda$), agrees well with the estimate based on model fitting the source structure.

The effect of correcting for the core elongation is illustrated in Fig. 5, where the correcting factor φ_ϵ is applied to brightness temperature estimates made from the visibility data on 3C 345 presented in Figs. 2-3. The corrections are derived for an axial ratio $\epsilon = 0.5$ (weighted average of the model-fitting results in Kovalev et al. 2005) and a jet position angle $\psi_{\text{jet}} = -104^\circ$ inferred from the source structure shown in Fig. 2. The increased scatter at shorter baselines shows the effect of contributions from larger structures that are incorrectly described by the adopted values of ϕ_{jet} and, in particular, ϵ . However, at the longest baselines, correcting for the core elongation clearly improves the $T_{b,\text{lim}}$ estimate and brings it well within the errors of the model-fit-based estimate. The same correction applied to NGC 1052 (with $\epsilon = 0.4$ and $\psi_{\text{jet}} = -110^\circ$) results in corrected $T_{b,\text{min}} = 1.1 \times 10^{10}$ K and $T_{b,\text{lim}} = 2.4 \times 10^{10}$ K, with the latter value falling very close to $T_{b,\text{mod}} = 2.8 \times 10^{10}$ K estimated from the modelfit. Both these results indicate that $T_{b,\text{lim}}$ can be improved by correcting for the elongation of the core region.

3. Discussion

Applying the visibility-based brightness temperature estimates to VLBI data on 3C 345 and NGC 1052 has demonstrated that the method is reliable in two particular cases. A more extended testing of the method can be performed on a statistical basis by applying it to visibility data from large VLBI survey programs aimed at measuring and analyzing the brightness temperature distribution in samples of compact radio sources. The analysis of fine scale structure in the 15 GHz ($\lambda_{\text{obs}} = 2 \text{ cm}$) MOJAVE sample (Kovalev et al. 2005) and the results of brightness temperature measurements from the 86 GHz ($\lambda_{\text{obs}} = 3 \text{ mm}$) CMVA survey Lee et al. (2008) offer statistically suitable samples for such tests. The MOJAVE analysis was based on elliptical Gaussian model fits of the core region. The 86 GHz data were fitted by circular Gaussian components. Resolution criteria were applied to the data from both surveys to constrain the core components

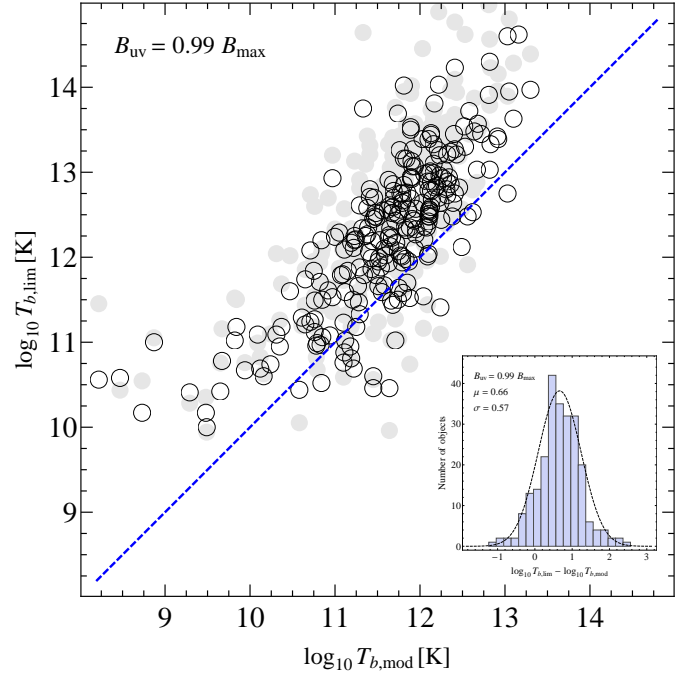


Fig. 6. Comparison of $T_{b,\text{lim}}$ (circular Gaussian approximation) and $T_{b,\text{mod}}$ estimates obtained from the MOJAVE data (open circles). Gray circles illustrate the effect of correcting $T_{b,\text{lim}}$ for the putative elongation of the core region. The dashed line marks the one-to-one correspondence between the two estimates. For each object, the $T_{b,\text{lim}}$ is estimated from MOJAVE data at $B_{\text{uv}} \geq 0.99 B_{\text{max}}$ to restrict the visibility information to the most compact structures. The resulting $T_{b,\text{lim}}$ are on average 4.6 times higher than $T_{b,\text{mod}}$. The residual logarithmic distribution of the $T_{b,\text{lim}}/T_{b,\text{mod}}$ ratio (inset) can be approximated by the Gaussian PDF with $\mu = 0.66$ and $\sigma = 0.57$. At $T_{b,\text{mod}} \lesssim 10^{10}$ K the $T_{b,\text{lim}}$ may be biased by large-scale structure contributions in strongly jet-dominated objects.

with degenerate size parameters (circular diameter or one of the two axes of elliptical Gaussian) obtained from the model fitting.

3.1. Preparation of the visibility data

To evaluate the performance of visibility-based brightness temperature limits on a self-consistent statistical basis, visibility data for each source from these two programs (244 objects in the MOJAVE sample and 123 observations of 109 individual objects in the CMVA sample) were radially and azimuthally averaged within a small annulus, $(B_{\text{uv}}, B_{\text{max}})$ in the uv plane. The purpose of clipping the data is to reduce the adverse effect of including shorter baselines that are dominated by extended structure. The upper limit of the annulus is determined by the longest baseline B_{max} found in the data for each individual object. The MOJAVE datasets were clipped at $B_{\text{uv}} = 0.99 B_{\text{max}}$ (i.e., in an annulus located within 1% of B_{max}). The CMVA survey data, with substantially fewer visibilities per target object, were clipped at $B_{\text{uv}} = 0.9 B_{\text{max}}$. The resulting average uv distances and visibility position angles in the clipped data are $435 \pm 27 \text{ M}\lambda$ and $-88^\circ \pm 6^\circ$ for the MOJAVE data and $2270 \pm 660 \text{ M}\lambda$ and $-78^\circ \pm 20^\circ$ for the CMVA data. In each case, the fraction of visibilities selected is $\sim 1/N_{\text{bas}}$, where N_{bas} is the number of baselines in a dataset. Following the conclusions obtained from analyzing the data on 3C 345 and NGC 1052, these uv distances should be sufficiently long to reduce the visibility contamination by large-scale structures to negligible levels. The $T_{b,\text{lim}}$ estimates were therefore

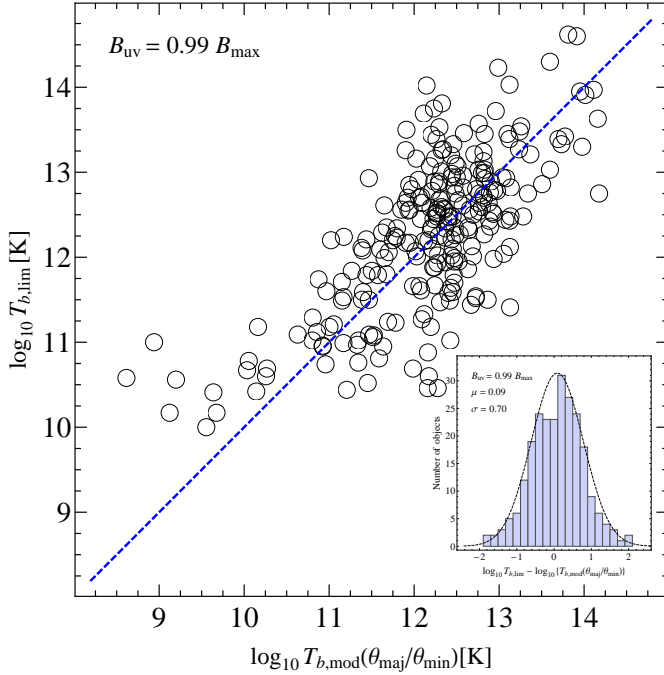


Fig. 7. Correlation between $T_{b,lim}$ and $T_{b,mod}(\theta_{maj}/\theta_{min})$ expressing the brightness temperature obtained assuming that the characteristic size of the brightest region is determined by the jet transverse dimension as given by the minor axis of the elliptical Gaussian fit. The average $T_{b,lim}$ is only 20% higher than the respective corrected values of $T_{b,mod}$, and the residual logarithmic distribution of the $T_{b,lim}/T_{b,mod}$ ratio (inset) can be approximated by the Gaussian PDF with $\mu = 0.09$ and $\sigma = 0.70$.

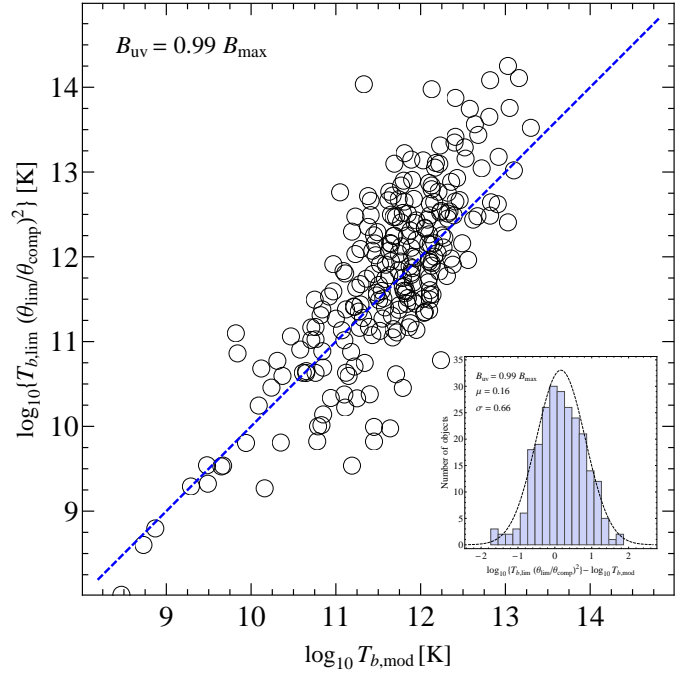


Fig. 8. Correction of the distribution shown in Fig. 6 for the square of the resolution factor $\theta_{lim}/\theta_{comp}$. The corrected $T_{b,lim}$ distribution is statistically very close to the $T_{b,mod}$ obtained from the model-fitting analysis. The values of $T_{b,lim}$ are on average 40% higher than the respective values of $T_{b,mod}$. This is also demonstrated by the residual logarithmic distribution of the $T_{b,lim}/T_{b,mod}$ ratio (inset), which can be approximated by the Gaussian PDF with $\mu = 0.16$ and $\sigma = 0.66$.

calculated for each source from all of the visibilities clipped and averaged within the respective annuli. The circular Gaussian approximation was used in these calculation.

3.2. Results from the MOJAVE data

For the MOJAVE data, the resulting estimates of $T_{b,lim}$ are compared in Fig. 6 with the $T_{b,mod}$ estimates obtained in Kovalev et al. (2005) for each source at the same observing epoch. The two estimates agree reasonably well, with $T_{b,lim}$ being on average 4.6 times higher than the respective $T_{b,mod}$. This is similar to the $T_{b,lim}/T_{b,mod}$ ratios measured in 3C 345 and NGC 1052. Overall, the $T_{b,lim}$ estimates provide a reasonable upper bound on the brightness temperature, with the scatter in the estimates limited to about half a decade over nearly five orders of magnitude in brightness temperature.

Correction for the putative elongation of the core region has been attempted for the MOJAVE data, based on the elliptical model fits and measured position angles of the jet. The elongation was calculated as the ratio of the minor to major axes of the elliptical Gaussian component describing the core. Two options were tried for the jet position angle: a) the position angle of the major axis of the Gaussian component, and b) the average position angle of the jet as reported in Kovalev et al. (2005). The results of applying the elongation correction with the former option are shown in Fig. 6. Neither of the two corrections has improved the correlation for either the average $T_{b,lim}/T_{b,mod}$ ratio or the spread of the residuals.

This result may be caused by two factors. On the one hand, it may suggest that the elongation of the core region is not ac-

curately reflected in the parameters of the elliptical Gaussian components, for instance, if this region has a specific geometry such as a conically expanding jet (cf. Blandford & Königl 1979) or a jet pervaded with thread-like instability patterns (cf. Lobanov & Zensus 2001). On the other hand, the lack of improvement achieved with the elongation correction may indicate that the highest brightness is realized in a region that is smaller than the major axis of the Gaussian component describing the core region. Again, this would be the case for a quasi-stationary conical jet or a jet dominated by the instability patterns. In each of these situations, the observed jet brightness would be largely determined by its transverse dimension. If this is the case, $T_{b,lim}$ could be reconciled with $T_{b,mod}$ derived under the assumption that only the minor axis, θ_{min} , of the Gaussian component is relevant for determining the jet brightness.

This hypothesis is tested in Fig. 7 by comparing $T_{b,lim}$ to $T_{b,mod} \theta_{maj}/\theta_{min}$, which has the effect of calculating the size of the core region as $\pi \theta_{min}^2/4$. This simple correction brings the two estimates to a very good agreement, with $T_{b,lim}$ estimates, as demonstrated by both the average ratio between the two estimates and the distribution of logarithmic residuals of this ratio. The only notable discrepancy between the two estimates is the persistently higher $T_{b,lim}$ values observed for the low $T_{b,mod} \lesssim 3 \times 10^{10}$. Such brightness temperatures are typically measured in objects in which the cores are strongly resolved along both axes of the fitted Gaussians, hence they may require a correction for the resolution along the minor axis of the Gaussian as well.

Such a correction can be performed by substituting the fitted effective size, $\theta_{comp} = \sqrt{\theta_{min}\theta_{maj}}$ of the Gaussian component with its respective resolution limit θ_{lim} derived in Kovalev et al.

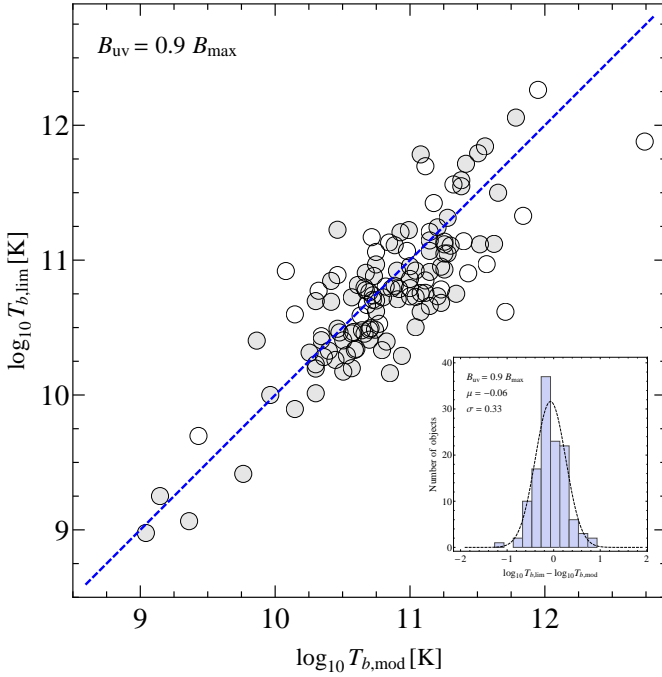


Fig. 9. Comparison of $T_{b,\text{lim}}$ (circular Gaussian approximation) and $T_{b,\text{mod}}$ estimates obtained from the 86 GHz survey data (Lee et al. 2008). Open circles indicate objects with lower limits on $T_{b,\text{mod}}$. The dashed line marks the one-to-one correspondence between the two estimates. For each object, the $T_{b,\text{lim}}$ is estimated from the 86 GHz data at $R_{\text{uv}} \geq 0.90 B_{\text{max}}$ to restrict the visibility information to the most compact structures. The resulting $T_{b,\text{lim}}$ are essentially equal to $T_{b,\text{mod}}$. The residual logarithmic distribution of the $T_{b,\text{lim}}/T_{b,\text{mod}}$ ratio (inset) can be approximated by the Gaussian PDF with $\mu = -0.06$ and $\sigma = 0.33$.

(2005). This operation should account for resolving the core region along and across the jet direction as marked by the position angle of the major axis of the fitted Gaussian component. Applying this correction is illustrated by Fig. 8, which shows an excellent agreement between the two estimates of the brightness temperature and indeed effectively brings the low $T_{b,\text{mod}}$ outliers to the main correlation trend.

The examples set by substituting the measured core size by either θ_{min} or θ_{lim} indicate that the visibility-based estimates of $T_{b,\text{lim}}$ can be related to brightness temperature estimates obtained from Gaussian model fitting and that the $T_{b,\text{lim}}$ estimates present a reliable account of brightness temperatures measured at the *limit of angular resolution* of the respective interferometric data sets.

3.3. Results from the CMVA survey data

If $T_{b,\text{lim}}$ is indeed determined by the limiting resolution of the data, the difference between the $T_{b,\text{lim}}$ and $T_{b,\text{mod}}$ estimates should become progressively smaller with increasing $q_{\text{max}} = B_{\text{max}}/\lambda_{\text{obs}}$ and for model fitting performed with circular Gaussian components (essentially forcing model fitting to be more responsive to the resolution limit). Both these conditions are fulfilled with the 86 GHz data from the CMVA survey.

An analysis of the 86 GHz survey data presented in Fig. 9 demonstrates that at spatial frequencies $q \geq 2 \text{ G}\lambda$, the estimates $T_{b,\text{lim}}$ and $T_{b,\text{mod}}$ yield similar brightness temperatures. This indicates that at these spatial frequencies, the visibility distribution is strongly dominated by the most compact struc-

ture, which is reflected both in the modelfit results and in the visibility-based estimates of $T_{b,\text{lim}}$. It can therefore be expected that the visibility-based estimates provide reliable brightness temperature limits for RadioAstron space VLBI measurements (Kardashev et al. 2013) and millimeter VLBI observations (Doeleman et al. 2012), reaching frequency spacings well in excess of $1 \text{ G}\lambda$.

3.4. Comparisons with $T_{b,\text{min}}$

Statistical comparisons of $T_{b,\text{mod}}$ and $T_{b,\text{lim}}$ with the minimum brightness temperature $T_{b,\text{min}}$ can also be made, although the latter estimate may be affected by a general flux density bias in the survey. We recall that $T_{b,\text{min}}$ only depends on the absolute value of the visibility amplitude, while $T_{b,\text{lim}}$ effectively represents the signal-to-noise ratio (SNR) of the visibility.

The average ratios of $T_{b,\text{lim}}/T_{b,\text{mod}}$ are $2.0^{+2.3}_{-1.1}$ and $1.6^{+0.7}_{-0.5}$ for the MOJAVE and CMVA samples, respectively. These values are similar to the ratios of 2.6 and 2.1 obtained in Sect. 2 from the full-track VLBI data on 3C 345 and NGC 1052. The rather large spread of these average ratios is indicative of random errors in the flux density scales of both surveys (which can result from self-calibration applied during imaging the survey data). The lower bounds of both averages are ≈ 1 , which can either reflect a relatively low SNR of the long-baseline visibilities or suggest that a systematic bias may also affect the flux density scales.

The average $T_{b,\text{lim}}/T_{b,\text{mod}}$ ratios imply $\text{SNR}_{\text{MOJAVE}} = 3.9$ and $\text{SNR}_{\text{CMVA}} = 2.8$ on the baselines at which the brightness temperature limits are estimated. This is indeed similar to the measured SNR on the longest baselines in the survey data.

The average SNR can also be used to calculate the amount of bias in the flux density scale that is needed to bring the survey results closer to the results from the two full-track cases considered. In both cases, a positive flux density bias of about 20% on the longest baselines would reconcile the survey averages with those of the full-track data. Hence, this can also be a viable possibility, in particular for the CMVA data that have been collected in three long observing runs.

The comparison of $T_{b,\text{min}}$ and $T_{b,\text{mod}}$ obtained from the MOJAVE data yields an average ratio $T_{b,\text{min}}/T_{b,\text{mod}} = 2.3$, while a ratio of ≤ 1 is expected. This discrepancy probably results from the same potential problems as discussed in Sect. 3.2 in connection with using elliptical modelfits to describe the core region. Indeed, applying either the θ_{min} or the θ_{lim} correction described in Sect. 3.2 reduces this ratio to 0.7. This lends further support to the conclusion that elliptical modelfits may not be optimal for estimating the brightness temperature in compact jets because it is effectively determined by the transverse dimension of the flow. Following this line of argument, the CMVA data (fitted by circular Gaussian and providing substantially longer baselines for estimating $T_{b,\text{min}}$) should yield a better value of the average $T_{b,\text{min}}/T_{b,\text{mod}}$ ratio. This is indeed the case, with the average $T_{b,\text{min}}/T_{b,\text{mod}} = 0.5$ measured from the CMVA data.

3.5. General implications for T_b measurements

Overall, the comparisons of $T_{b,\text{lim}}$ and $T_{b,\text{mod}}$ made using the MOJAVE and the CMVA survey data indicate that brightness temperature estimates obtained from the visibility flux density at longest baselines (highest spatial frequencies) provide suitable limits on the brightness temperature of the most compact emitting regions in radio sources. These comparisons also suggest that visibility-based estimates may even be more realistic in case

of complex structure of the emitting region (*i.e.*, a marginally transversely resolved flow, such as a compact conical jet, or a flow with thread-like patterns embedded).

The same situation may be realized for other types of objects studied with interferometric measurements, for instance, in radio interferometry observations of young supernovae (Marcaide et al. 2009), radio (Dyck et al. 1998) and optical (Cusano et al. 2012; Ohnaka et al. 2013; Arroyo-Torres et al. 2014) interferometry studies of resolved stars, and optical interferometry observations of protoplanetary disks (Malbet et al. 2005), recurrent novae (Chesneau et al. 2007), and active galaxies (Weigelt et al. 2012). In optical interferometry experiments that measure the normalized visibility spectrum V_q/V_0 , the zero-spacing flux, V_0 , may need to be determined in a separate measurement (*cf.* Cusano et al. 2012). In all of these cases, brightness temperature estimates can be made with a visibility response calculated for a specific pattern of brightness distribution (see Appendix A). For objects with a complex *internal* structure, this would correspond to estimating a *pattern-averaged* brightness temperature, while the brightness temperature of the most compact regions can still be estimated by using the data from the longest baselines and applying the generic Gaussian case described in Sect. 2.

The arguments presented above demonstrate that for a given interferometric measurement, a range of plausible brightness temperatures of the most compact emitting structure can be determined from the visibility amplitude and its error measured at the longest baselines contributing to the measurement. This procedure effectively addresses the brightness temperature of emitting regions detected at the limiting resolution of the measurement.

In summary, our analysis leads to the following basic conclusions about applying visibility data to constrain the brightness temperature in astrophysical objects:

1. A measurement of visibility amplitude, V_q , alone is sufficient to constrain the *minimum* brightness temperature, $T_{b,\min}$, that can be derived from this visibility under the assumption that the brightness distribution of the target object can be described by a Gaussian function. This holds for both circular and elliptical Gaussians and indeed for any visibility distribution that has an inflection point (for instance, for any visibility distribution that can be approximated by a Bessel function of the first kind).
2. If the brightness temperature of an emitting region with a putative Gaussian brightness distribution is constrained using an assumed limit on the zero-spacing flux density, V_0 , the nature of the resulting constraint depends on the ratio V_0/V_q . For $V_0 > e V_q$, lower/upper limits on V_0 provide lower/upper limits on T_b . For $V_0 < e V_q$, lower/upper limits on V_0 provide upper/lower limits on T_b .
3. A measurement of visibility amplitude, V_q , and its r.m.s. error, σ_q , can be used to calculate the *maximum* brightness temperature, $T_{b,\lim}$ that can be obtained under assumption that the emitting region is marginally resolved.
4. At spatial frequencies higher than $\sim 200 M\lambda$, the interval $[T_{b,\min}, T_{b,\lim}]$ provides a reliable bracketing for the brightness temperature of the most compact structure in the target object.
5. Applying the analysis to samples of radio sources with brightness temperatures derived from model fitting the compact structure indicates that the brightness temperature in the relativistic jets may be largely determined by the transverse dimension of the flow.

6. The visibility-based estimates of brightness temperature can offer a suitable tool for constraining this physical parameter in a wide range of experiments in which a full reconstruction of the source structure is not feasible.

Acknowledgments

This research has made use of data from the MOJAVE database that is maintained by the MOJAVE team (Lister et al., 2009, AJ, 137, 3718) and of data obtained with the Global Millimeter VLBI Array, which consists of telescopes operated by the MPIfR, IRAM, Onsala, Metsahovi, Yebes and the VLBA. The VLBA is an instrument of the National Radio Astronomy Observatory, a facility of the National Science Foundation operated under cooperative agreement by Associated Universities, Inc.

References

- Arroyo-Torres, B., Martí-Vidal, I., Marcaide, J. M., et al. 2014, A&A, 566, A88
 Berger, J.-P. 2003, in EAS Publications Series, Vol. 6, EAS Publications Series, ed. G. Perrin & F. Malbet, 23
 Blandford, R. D. & Königl, A. 1979, ApJ, 232, 34
 Chesneau, O., Nardetto, N., Millour, F., et al. 2007, A&A, 464, 119
 Cusano, F., Paladini, C., Richichi, A., et al. 2012, A&A, 539, A58
 Doleman, S. S., Fish, V. L., Schenck, D. E., et al. 2012, Science, 338, 355
 Dyck, H. M., van Belle, G. T., & Thompson, R. R. 1998, AJ, 116, 981
 Homan, D. C., Kovalev, Y. Y., Lister, M. L., et al. 2006, ApJ, 642, L115
 Horiuchi, S., Fomalont, E. B., Taylor, W. K., et al. 2004, ApJ, 616, 110
 Kardashev, N. S., Khartov, V. V., Abramov, V. V., et al. 2013, Astronomy Reports, 57, 153
 Kellermann, K. I., Lister, M. L., Homan, D. C., et al. 2004, ApJ, 609, 539
 Kovalev, Y. Y., Kellermann, K. I., Lister, M. L., et al. 2005, AJ, 130, 2473
 Lee, S.-S., Han, M., Kang, S., et al. 2013, in European Physical Journal Web of Conferences, Vol. 61, European Physical Journal Web of Conferences, 7007
 Lee, S.-S., Lobanov, A. P., Krichbaum, T. P., et al. 2008, AJ, 136, 159
 Lobanov, A. P., Krichbaum, T. P., Graham, D. A., et al. 2000, A&A, 364, 391
 Lobanov, A. P. & Zensus, J. A. 2001, Science, 294, 128
 Malbet, F., Lachaume, R., Berger, J.-P., et al. 2005, A&A, 437, 627
 Marcaide, J. M., Martí-Vidal, I., Alberdi, A., et al. 2009, A&A, 505, 927
 Ohnaka, K., Hofmann, K.-H., Schertl, D., et al. 2013, A&A, 555, A24
 Petrov, L., Lee, S.-S., Kim, J., et al. 2012, AJ, 144, 150
 Weigelt, G., Hofmann, K.-H., Kishimoto, M., et al. 2012, A&A, 541, L9

Appendix A: Visibility limits on the brightness temperature derived for specific patterns of brightness distribution

Visibility limits on brightness temperature can be obtained by combining the expression for brightness temperature,

$$T_b = \frac{h\nu}{k} \ln^{-1} \left(1 + \frac{2h\nu^3}{I(r)c^2} \right) = \frac{h\nu}{k} \ln^{-1} (1 + I_b) \\ \rightarrow \frac{I(r)c^2}{2k\nu^2} \quad \text{for } h\nu \ll kT, \quad (\text{A.1})$$

with the visibility function, V , calculated for a specific, circularly symmetric pattern of brightness distribution, $I(r)$, observed with an interferometer at a spatial harmonic, q , which yields a visibility measurement $V(q)$ and its r.m.s. error $\sigma(q)$. Here h is the Planck constant, k is the Boltzmann constant, c is the light speed, and ν is the frequency of measurement.

For the Planck regime, the term I_r is derived for each pattern. Full expressions for T_b are given for the Rayleigh-Jeans regime. The general form of brightness distribution pattern is chosen to be $I(r) = \eta_d S_{\text{tot}} f(r)$, where $S_{\text{tot}} \equiv V(0)$ is the total or zero-spacing intensity of the pattern, and $f(r)$ and η_d are the respective pattern-specific radial dependence of brightness and its normalization factor (generally dependent on the size d of

Table A.1. Visibility brightness temperature estimates for specific patterns of brightness distribution

| | Circular Gaussian component | Uniformly bright disk | Optically thin shell of finite thickness | |
|------------------------|--|---|--|---|
| | | | shell average | peak brightness |
| I_r | $\frac{2\sqrt{\ln 2}}{\sqrt{\pi}} \frac{S_{\text{tot}}}{d} \exp\left(-\frac{4\ln 2 r^2}{d^2}\right)$ | $S_{\text{tot}} \begin{cases} 4/(\pi d^2), & r \leq d/2, \\ 0 & r > d/2 \end{cases}$ | $I_0 \begin{cases} (d^2 - 4r^2)^{1/2} - (\alpha^2 d^2 - 4r^2)^{1/2} & 2r < \alpha d, \\ (d^2 - 4r^2)^{1/2} & \alpha d \leq 2r \leq d, \\ 0 & 2r > d, \end{cases}$ with $I_0 = \frac{6S_{\text{tot}}}{\pi d^3(1 - \alpha^3)}$ | |
| T_b | $\frac{2\ln 2}{\pi k} \frac{S_{\text{tot}} \lambda^2}{d^2}$ | $\frac{2}{\pi k} \frac{S_{\text{tot}} \lambda^2}{d^2}$ | $\frac{2}{\pi k} \frac{S_{\text{tot}} \lambda^2}{d^2}$ | $\frac{3}{\pi k} \frac{S_{\text{tot}} \lambda^2}{d^2(1 - \alpha^3)^{1/2}}$ |
| \mathcal{I}_b | $\frac{\pi h \nu}{2\ln 2} \frac{d^2}{S_{\text{tot}} \lambda^2}$ | $\frac{\pi h \nu}{2} \frac{d^2}{S_{\text{tot}} \lambda^2}$ | $\frac{\pi h \nu}{2} \frac{d^2}{S_{\text{tot}} \lambda^2}$ | $\frac{\pi h \nu}{3} \frac{d^2(1 - \alpha^3)^{1/2}}{S_{\text{tot}} \lambda^2}$ |
| V_q | $V_0 \exp\left(-\frac{\pi^2 q^2 d^2}{4\ln 2}\right)$ | $V_0 \frac{2J_1(\pi d q)}{\pi d q} \approx$ $\approx V_0 \left(1 - \frac{\pi^2 d^2 q^2}{8}\right)$ | $V_0 \frac{3}{(1 - \alpha^3)\pi^3 d^3 q^3} [\sin(\pi d q) - \pi d q \cos(\pi d q) -$ $- \sin(\alpha \pi d q) + \alpha \pi d q \cos(\alpha \pi d q)] \approx$ $\approx V_0 \left(1 - \frac{\pi^2 d^2 q^2}{10} \frac{1 - \alpha^5}{1 - \alpha^3}\right)$ | |
| d_q | $\frac{2\sqrt{\ln 2}}{\pi} \frac{1}{q} \sqrt{\ln(V_0/V_q)}$ | $\frac{2\sqrt{2}}{\pi q} \sqrt{1 - V_q/V_0}$ | $\frac{\sqrt{10}}{\pi q} \left(\frac{1 - \alpha^3}{1 - \alpha^5}\right)^{1/2} \sqrt{1 - V_q/V_0}$ | |
| $T_{b,q}$ | $\frac{\pi}{2k} \frac{B^2 V_0}{\ln(V_0/V_q)}$ | $\frac{\pi}{4k} \frac{B^2 V_0^2}{V_0 - V_q}$ | $\frac{\pi}{5k} \frac{1 - \alpha^5}{1 - \alpha^3} \frac{B^2 V_0^2}{V_0 - V_q}$ | $\frac{3\pi}{10k} \frac{1 - \alpha^5}{(1 - \alpha^3)^{3/2}} \frac{B^2 V_0^2}{V_0 - V_q}$ |
| $\mathcal{I}_{b,q}$ | $\frac{2h\nu}{\pi} \frac{\ln(V_0/V_q)}{B^2 V_0}$ | $\frac{4h\nu}{\pi} \frac{V_0 - V_q}{B^2 V_0^2}$ | $\frac{5h\nu}{\pi} \frac{1 - \alpha^3}{1 - \alpha^5} \frac{V_0 - V_q}{B^2 V_0^2}$ | $\frac{10h\nu}{3\pi} \frac{(1 - \alpha^3)^{3/2}}{1 - \alpha^5} \frac{V_0 - V_q}{B^2 V_0^2}$ |
| $T_{b,\min}$ | $\frac{\pi e}{2k} B^2 V_q$ | $\frac{\pi}{k} B^2 V_q$ | $\frac{4\pi}{5k} \frac{1 - \alpha^5}{1 - \alpha^3} B^2 V_q$ | $\frac{6\pi}{5k} \frac{1 - \alpha^5}{(1 - \alpha^3)^{1/2}} B^2 V_q$ |
| $\mathcal{I}_{b,\min}$ | $\frac{2h\nu}{\pi e B^2 V_q}$ | $\frac{h\nu}{\pi B^2 V_q}$ | $\frac{5h\nu}{4\pi} \frac{1 - \alpha^3}{1 - \alpha^5} \frac{1}{B^2 V_q}$ | $\frac{5h\nu}{6\pi} \frac{(1 - \alpha^3)^{3/2}}{1 - \alpha^5} \frac{1}{B^2 V_q}$ |
| $T_{b,\lim}$ | $\frac{\pi}{2k} \frac{B^2 (V_q + \sigma_q)}{\ln[(V_q + \sigma_q)/V_q]}$ | $\frac{\pi}{4k} \frac{B^2 (V_q + \sigma_q)^2}{\sigma_q}$ | $\frac{\pi}{5k} \frac{1 - \alpha^5}{1 - \alpha^3} \frac{B^2 (V_q + \sigma_q)^2}{\sigma_q}$ | $\frac{3\pi}{10k} \frac{1 - \alpha^5}{(1 - \alpha^3)^{3/2}} \frac{B^2 (V_q + \sigma_q)^2}{\sigma_q}$ |
| $\mathcal{I}_{b,\lim}$ | $\frac{2h\nu}{\pi} \frac{\ln[(V_q + \sigma_q)/V_q]}{B^2 (V_q + \sigma_q)}$ | $\frac{4h\nu}{\pi} \frac{\sigma_q}{B^2 (V_q + \sigma_q)^2}$ | $\frac{5h\nu}{\pi} \frac{1 - \alpha^3}{1 - \alpha^5} \frac{\sigma_q}{B^2 (V_q + \sigma_q)^2}$ | $\frac{10h\nu}{3\pi} \frac{(1 - \alpha^3)^{3/2}}{1 - \alpha^5} \frac{\sigma_q}{B^2 (V_q + \sigma_q)^2}$ |

Notes: I_r – brightness distribution function; T_b – brightness temperature estimated from I_r ; V_q – visibility function; d_q – pattern size, estimated from the visibility ratio V_q/V_0 ; $T_{b,q}$ – brightness temperature corresponding to d_q ; $T_{b,\min}$ – minimum brightness temperature, obtained with $V_0 = e V_q$ for the Gaussian component and $V_0 = 2 V_q$ for the disk and the shell; $T_{b,\lim}$ – limiting brightness temperature, obtained with $V_0 = V_q + \sigma_q$. For the brightness temperature estimates, the respective \mathcal{I} expression give the \mathcal{I}_b term in the Planck form of the brightness temperature equation.

the pattern). The normalization, η_d , is chosen so that it provides a Fourier transform $\mathcal{F}I(r)$ of the form $V(q) = V(0)\mathcal{F}f(r)$. To simplify the expressions derived, I_r , V_0 and (V_q, σ_q) denote $I(r)$, $V(0)$ and $(V(q), \sigma(q))$ in the discussion below.

With the adopted normalization, a generic solution for the size d_q of the pattern can be determined by solving $\mathcal{F}I_r = V_q/V_0$ for d . The minimum brightness temperature supported by the visibility measurement V_q is obtained by substituting I_r with $I_r(d \rightarrow d_q)$ in Eq. A.1 and finding the value of V_0 that minimizes the respective T_b given by this equation (e.g., deriving V_0 from the condition $dT_b/dV_0 = 0$).

To derive the maximum measurable brightness temperature, the characteristic size, d_{\lim} , of the pattern is obtained from the relation $\mathcal{F}I_r = V_q/(V_q + \sigma_q)$. The maximum measurable brightness temperature $T_{b,\lim}$ is then calculated by substituting I_r in Eq. A.1 with $I_r(d \rightarrow d_{\lim})$.

Results of the calculations are presented in Table A.1 for a circular Gaussian component, a disk of uniform brightness, and a spherical shell of finite thickness. The characteristic size d represents, respectively, the full width at half maximum of the Gaussian component, the diameter of the disk, and the outer diameter of the shell. The spherical shell is further defined by its thick-

ness $\delta_r = (1 - \alpha)d/2$ (with $0 \leq \alpha \leq 1$). Thus, $\alpha = 0$ describes an infinitely thin shell and $\alpha \rightarrow 1$ describes a filled, optically thin sphere. Calculations for the spherical shell are made separately for the average shell brightness and for the peak brightness $I_{r,\text{peak}}$ in the shell, realized at $r = \alpha d/2$, with the resulting $I_{r,\text{peak}} = 6 S_{\text{tot}}/\pi d^2 (1 - \alpha^3)^{1/2}$.